Open access • Journal Article • DOI:10.1007/S00603-016-1116-8

Analysis of a Large Rock Slope Failure on the East Wall of the LAB Chrysotile Mine in Canada: Back Analysis, Impact of Water Infilling and Mining Activity — Source link

Martin Grenon, Philippe Caudal, Sina Amoushahi, Dominique Turmel ...+1 more authors

Institutions: Laval University

Published on: 01 Feb 2017 - Rock Mechanics and Rock Engineering (Springer Vienna)

Topics: Slope stability, Pit water and Open-pit mining

Analysis of a Large Rock Slope Failure on the East Wall of the LAB Chrysotile Mine in Canada: Back Analysis, Impact of Water Infilling and Mining Activity

Grenon M, Caudal P, & Amoushahi S
Faculté des sciences et de génie, Département de génie des mines, de la métallurgie et des matériaux, Université Laval, Québec, Canada

Turmel D & Locat J
Faculté des sciences et de génie, Département de géologie et de génie géologie, Université Laval, Québec, Canada

ABSTRACT
A major mining slope failure occurred in July 2012 on the East wall of the LAB Chrysotile mine in Canada. The major consequence of this failure was the loss of the local highway (Road 112), the main commercial link between the region and the Northeast USA. LiDAR scanning and subsequent analyses were performed and enabled quantifying the geometry and kinematics of the failure area. Using this information, this paper presents the back analysis of the July 2012 failure. The analyses are performed using deterministic and probabilistic limit equilibrium analysis and finite-element shear strength reduction analysis modelling. The impact of pit water infilling on the slope stability is investigated. The impact of the mining activity in 2011 in the lower part of the slope is also investigated through a parametric analysis.

KEYWORDS
Open pit mining, Slope stability, Numerical modelling, Case study, Deterministic and probabilistic analysis

CITATION
Grenon, M., Caudal, P., Amoushahi, S., Turmel, D., & Locat, J. (2017). Analysis of a Large Rock Slope Failure on the East Wall of the LAB Chrysotile Mine in Canada: Back Analysis, Impact of Water Infilling and Mining Activity. Rock Mechanics and Rock Engineering, 50(2), 403-418. doi:10.1007/s00603-016-1116-8

This is the author's version of the original manuscript.
The final publication is available at Springer Link Online via https://link.springer.com/article/10.1007/s00603-016-1116-8

1 INTRODUCTION

During the last century, the Chaudière-Appalaches region, in southern Québec, Canada, was a major world producer of asbestos, the source of the region's wealth. Nowadays, no asbestos mines are in operation in Québec; nevertheless, mine residues in the form of large open pits and their associated tailings characterize the region's landscape.

Road 112 is the most important public highway in the region, acting as the major commercial link between the region and the Northeast USA. This road was located immediately adjacent to the crest of the East wall of the LAB Chrysotile mine. In July 2012, a major slope failure occurred on this wall of the pit, taking with it a large portion of Road 112. During this failure, a vertical movement of 70 m was observed. The lateral extent of the failure was 1.1 km with an associated volume of 25 hm^3. At time of failure, the pit was no longer in operation, and the water level in the pit was rising because all water pumping had ceased.

This paper will present back analyses of this large failure. Making use of LiDAR data, the paper will present how the authors acquired accurate knowledge of the pre- and post-failure slope geometry and through field and laboratory testing determined practical ranges of strength values for the host rock masses. The paper will also present the results of using limit equilibrium analysis (LEA) and finite-element shear strength reduction analysis (FE-SSR) to reproduce the slope failure. It will also show the results of conducted Monte Carlo probability-of-failure analyses, using both LEA and FE-SSR, to show the influence of variable strength properties, mining at the toe in 2011, and a rising water table, thereby better understanding the mechanism involved at the time of failure. These types of probabilistic analysis of slope failure are not routinely conducted and compared. The paper presents a unique, well-documented case study that enables acquiring some valuable knowledge on the back analysis process for large slope failures.

2 CASE STUDY

The localization of LAB Chrysotile mine and the adjacent Road 112—on its east side—are shown in Fig. 1. Further details about the location and history of the mine are presented in Caudal et al. (2016). This section will present the slope and failure geometry, and the geological and mechanical properties of the various lithologies on the East wall of the pit.

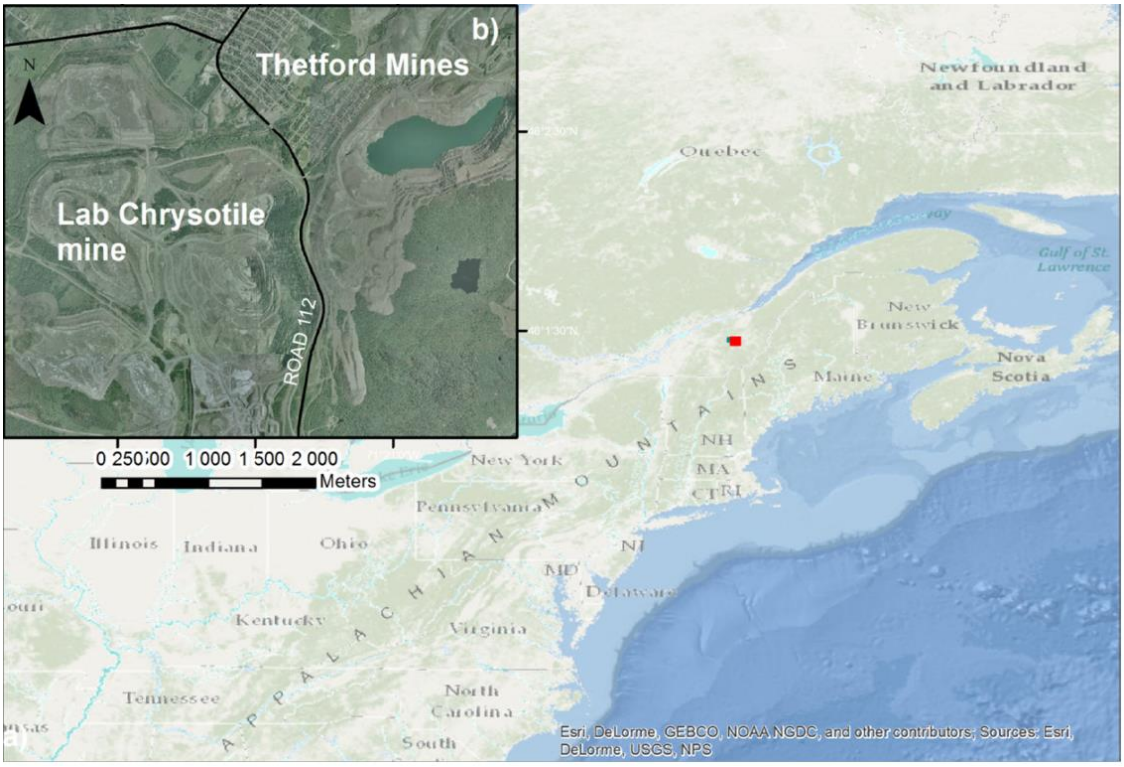

Figure 1. Localization of the LAB Chrysotile mine

2.1 East Wall Slope and Failure Geometry

Between 2010 and 2014, LiDAR monitoring of the East wall of the LAB Chrysotile open pit was performed on a regular basis (Caudal et al. 2016). This monitoring enabled defining the geometrical properties of the slope before, during and after the failure that occurred on this wall.

Four typical sections of the East wall were used for slope design at the mine site (Bonin 2013). To work in accordance with the mine site data, the pre-failure topography of the East wall was extracted from the digital terrain model (DTM) obtained on 29 June 2012 for these sections. The location of these sections is shown on the 29 June 2012 DTM (Fig. 2). These profiles are spaced 122 m apart, oriented and located according to cutting planes oriented at 90°/160° (dip/dip direction convention). The mine's naming convention was retained in the paper: E1, E2, E3 and E4.

LiDAR scanning provides accurate information on the topography of the East wall. The measurements of the wall were performed on all profiles (E1 to E4) and are presented in Fig. 3. These four profiles provide the geometric parameters of the East wall. The global slope ranges between 36° and 43°. The slope height is approximately 330 m. The road width varies from 85 to 94 m. One can also notice the waste rock, which was left by the neighbouring mine on the natural terrain more than 50 years ago.

Concerning the altitude of the water level at the bottom of the pit, it is measured at -14.7 m from the DTM of 11 July 2012 the day before the East wall failure. According to the mine restoration plan, the elevation of the lake outlet will be at an altitude of 233 m. This outlet will be created anthropically, and the outlet will reach a river nearby. Assuming that the water table line is 233 m, the pit should thus be filled by 2035, based on the infilling rate calculated from LiDAR monitoring. Lastly, at the time of the slope failure, the water table angle from the bottom of the pit was established at 23° based on field observations and initial numerical modelling, Caudal (2013, 2015).

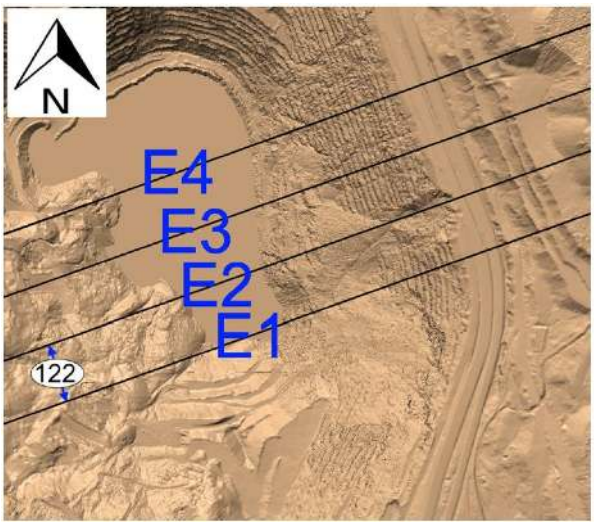

Figure 2. East wall of LAB Chrysotile mine: DTM of 29 June 2012 (all units are in metres unless stated otherwise)

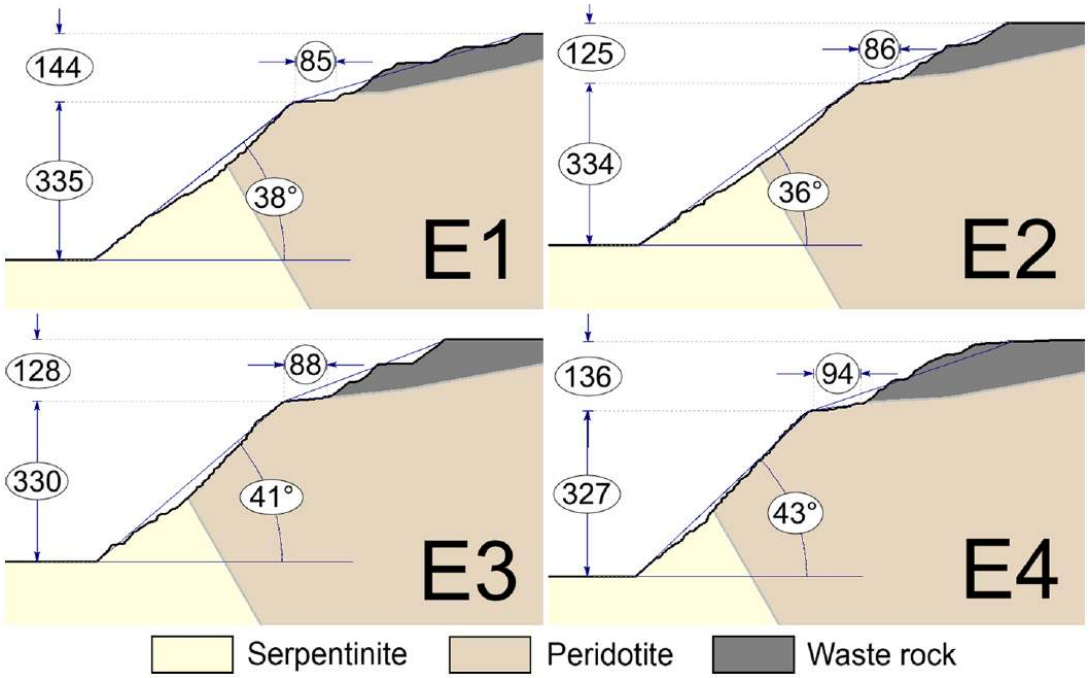

Figure 3. Geometric measurement of the East wall for profiles E1, E2, E3 and E4 extracted from the DTM obtained on 29 June 2012 (cutting planes oriented 90°/160°) (all units are in metres unless stated otherwise)

Table 1. Total displacement—orientation and magnitude—LiDAR quantification on a sector basis

Sector ID	Trend/plunge of mean displacement vector	Magnitude of total displacement (m)			
		From 22 Nov 2010 to 13 July 2012	From 13 July 2012 to 12 Nov 2012	From 12 Nov 2012 to 08 Nov 2013	From 08 Nov 2013 to 04 Nov 2014
1	275°/55°	66	22	27	0
2	270°/45°	65	24	20	0
3	280°/45°	54	16	24	0
4	260°/06°	56	21	18	0

2.2 East Wall Slide Geometry and Displacement

The failure, which happened in the East wall, took away a large section of Road 112, approximately 800 m long and 100 m wide. The north portion and part of the south portion of the failure moved in a quasi-monolithic way over a vertical distance of 70 m, and the displaced volume is estimated to be around a 25 hm^3. A summary of the slide geometry and displacement is presented in this subsection. For a detailed discussion of the East wall LiDAR monitoring, refer to Caudal et al. (2016).

Figure 4 presents the sector subdivision used to study the rock slope failure. Table 1 presents the results of the LiDAR-based total displacement analysis. The results indicate that the top part of the sliding was moving at a plunge of 55° while the bottom part of the slide was moving at a very shallow plunge angle. The total displacement magnitudes for all sectors were above 100 m and below 120 m.

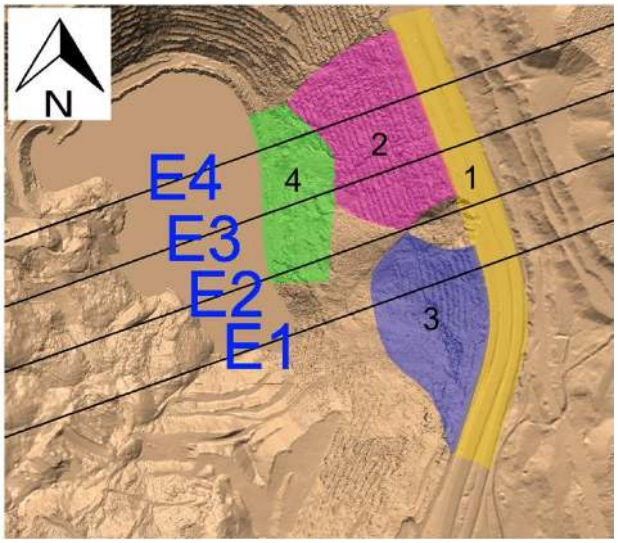

Figure 4. Subdivision of the East slope in four sectors

2.3 Location and Dip of the Upper Part

The geometry of the upper part of the failure was established based on LiDAR survey results. The dip of the upper part of the failure surface can be measured as shown in Fig. 5. The measurement of this angle was performed on the E1 to E4 cross sections extracted from the post-failure DTM recorded on 12 November 2012. The results of these measurements are summarized in Table 2. The dips vary between 45° and 71°. The height of the zone is approximatively 70 m for all sections. The distance of the failure zone to the crest was also quantified using LiDAR data. From Table 2, it can be seen that this distance varies from 46 to 83 m.

2.4 Detailed East Wall Lithology

All . The major lithological units are presented in Fig. 3. They consist of peridotite and serpentinite. Serpentinite is associated with the ore zone, while peridotite is the host rock. Table 3 presents a general geological description of these main units on the East wall.

A more detailed definition of the geometry of the lithological units (sections E1–E4) based on geotechnical drilling performed by the mine personnel on the East wall of the main pit (Bonin 2013) is given in Fig. 6. This figure shows the different sub-lithological units on these four sections. Serpentinite is presented in terms of mineralization, and peridotite depends on its degree of fracturing. The basis for this subdivision by the mine operator was rock mass mechanical properties. Peridotite rock mass properties are directly linked to their fracturing intensity. Engineers at the site have thus distinguished massive and fractured peridotite. Serpentinite rock mass properties are directly linked to their level of mineralization. Engineers at the site distinguished serpentinite based on its more or less strong mineralization, and thus, serpentinite was divided into four distinct rock types: massive serpentinite (non-mineralized serpentinite), weakly schistose serpentinite (mineralization below 50 %), semischistose (mineralization greater than 50 %) and schistose (100 % mineralization).

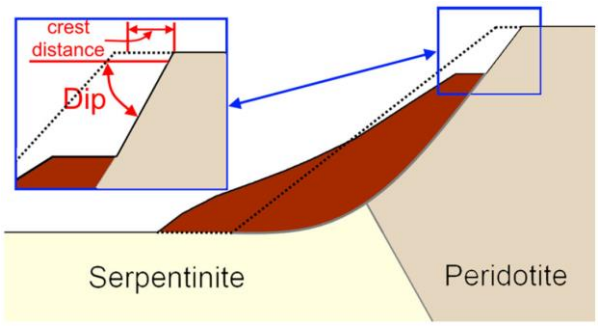

Figure 5. Upper failure geometry quantification from LiDAR scanning

Table 2. Location and geometry of the upper surface failure obtained from the DTM recorded on 12 November 2012

Date	Profile	Dip (°)	Crest distance (m)
12 Nov 2012	E1	45	83
	E2	52	61
	E3	71	65
	E4	60	46

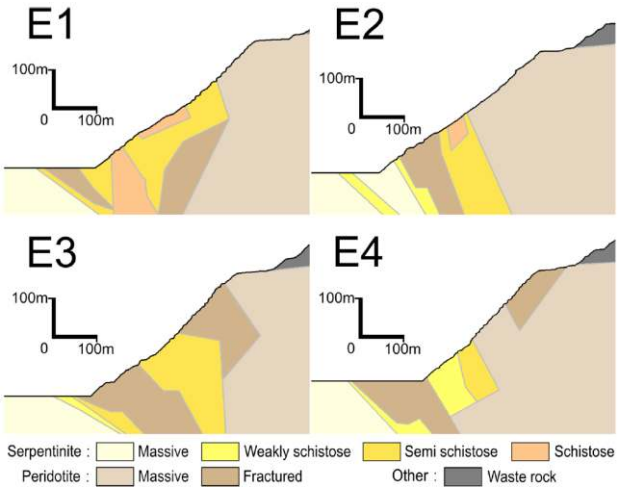

Figure 6. Lithologies for E1, E2, E3 and E4 sections after Bonin (2013)

Table 3. Geological description of major lithological units and summary of their rock mass properties

Unit	Geological description	Rock mass characteristics
Peridotite	A post-Ordovician intrusive rock consisting mainly of olivine and pyroxene with alteration to serpentinite; the unaltered olivine crystals are about 0.5 mm in diameter	A hard and strong rock with UCSi varying from 70 to 237 MPa
	Massive, unaltered to weakly serpentinized	Hoek and Brown mi between 20 and 30
	Fractures with calcite and chlorite or asbestos (chrysotile) coatings	Unit weight (kN/m^3) 27.5
		Rock mass described as being moderately to massively fractured (GSI 37–75)
Serpentinite	Semi-schistose to schistose; coated by fibrous minerals, with evidence of shearing	Moderately weak rock with UCSi varying from 30 to 37 MPa
		Hoek and Brown mi between 10 and 14
		Unit weight (kN/m^3) 25.1
		Rock mass described as being highly fractured (GSI 17–58)

2.5 Rock Mass Properties

In this paper, based on historical failures at the mining site, large-scale failures are assumed to occur throughout the highly fractured rock mass. It is thus deemed adequate to use an equivalent continuum approach to represent the rock mass properties.

Rock mass properties were derived for each of the lithologies presented in Sect. 2.4. This involved compiling data from mine geotechnical reports in which laboratory testing and rock mass characterization data were reported. Because these reports span several different testing and field characterization campaigns (over a period of more than 50 years), all data were reviewed and evaluated to establish lower and upper bound values. This work was enhanced by field and laboratory-based assessments made by the authors during fieldwork carried out at the mine site between 2012 and 2014. The rock mass descriptions and rock strengths provided are compiled from several modelling, laboratory testing and field measurement sources. Table 3 presents for serpentinite and peridotite ranges of values obtained for uniaxial compressive strength of intact rock (UCSi), Hoek–Brown rock parameter (mi), geological strength index (GSI) and unit weight.

As performed and explained by Woo et al. (2012), from these field and laboratory data, rock mass shear strength properties are estimated to define a Mohr–Coulomb perfectly plastic constitutive model. These authors also state that most practitioners have more experience and therefore an intuitive feeling for the physical meanings of cohesion and friction on which the Mohr–Coulomb criterion is based. Accordingly, Mohr–Coulomb rock mass shear strength properties for use in numerical analysis were derived through empirical procedures based on GSI, UCSi and mi. Several empirical procedures exist to derive Mohr–Coulomb rock mass shear strength properties; one of the most commonly used is the Hoek et al. (2002) conversion achieved by fitting an average linear relationship to the nonlinear Hoek–Brown envelope for a range of minor principal stress values with an upper bound of $\sigma_3$max. Analytical relationships are provided by these authors for estimating $\sigma_3$max.

From preliminary analysis and LiDAR results, the depth of the critical failure surface within the rock mass was estimated for all lithologies in all sections. $\sigma_3$max was estimated on these bases. Table 4 presents the mean failure depths estimated from preliminary analysis, Caudal (2013, 2015).

Table 5 reports the corresponding ranges of equivalent rock mass cohesion and friction angle values for the lower and upper bound scenarios covering the large spectrum of gathered rock mass properties. The average values represent the mean conditions of these properties. To capture the variability in the various rock mass properties, the normal (Gaussian) distribution was used. This distribution is the most common type of probability density function and is generally used for probabilistic studies in geotechnical engineering. For a normal distribution, 99.73% of all samples fall within three standard deviations (SDs) of the mean value. The standard deviation established for each lithological unit involved in the analyses is also presented in Table 5.

A gradation was used in selecting the average input values for all properties based on the range previously presented in Table 3. For example, the mean GSI for schistose serpentinite had to be lower than the values used for all other type of serpentinite. The average value for massive serpentinite had to be higher than any other serpentinite mean GSI value.

Table 4. Average depth of surface failure for each lithological unit

Lithology		Average depth (m)
Geological	Geomechanical	
Peridotite	Massive	104
	Fractured	92
Serpentinite	Massive	50
	Weakly schistose	81
	Semi-schistose	103
	Schistose	37

Table 5. Mohr Coulomb rock mass properties for East wall lithologies

Lithology		Rock mass	
Geological	Geotechnical	c (kPa)	φ (°)
Peridotite	Massive	Min: 430	Min: 34
		Avg: 566	Avg: 37
		Max: 2200	Max: 56
		SD: 75	SD: 3.5
	Fractured	Min: 430	Min: 34
		Avg: 459	Avg: 35
		Max: 2200	Max: 56
		SD: 75	SD: 3.5
Serpentinite	Massive	Min: 50	Min: 11
		Avg: 176	Avg: 29.5
		Max: 475	Max: 42
		SD: 75	SD: 3.5
	Weakly schistose	Min: 50	Min: 11
		Avg: 176	Avg: 21
		Max: 475	Max: 42
		SD: 75	SD: 3.5
	Semi-schistose	Min: 50	Min: 11
		Avg: 190	Avg: 19
		Max: 475	Max: 42
		SD: 75	SD: 3.5
	Schistose	Min: 50	Min: 11
		Avg: 88	Avg: 23
		Max: 475	Max: 42
		SD: 75	SD: 3.5

3 BACK ANALYSIS

3.1 Geometrical Properties of the Models

A back analysis was performed to better define possible ranges of rock mass properties for the various units and to better understand the behaviour of the rock slope. Figure 7 presents the geometrical properties considered in the analysis and introduced in Sect. 2. The water table line is presented in blue; the elevation of the water table behind the slope is at 250 m. This level is slightly higher than the 233 m evaluated in Sect. 2 and represents a worst-case scenario. The failure's initial location estimation is shown in red. Failure surface dip and location behind the crest were estimated based on LiDAR measurements and presented in Sect. 2. The failure surface was arguably assumed to be daylighting at the toe of the slope based on field observations. The elevation of the water in the pit is -14.7 m.

3.2 LEA—FoS and PoF Results

This section presents a back analysis of the slope failure using the limit equilibrium method as implemented in Slide v7.2D, Rocscience Inc. (2016a). The objective of this section is to compute the factor of safety (FoS) associated with the critical failure surface derived from field monitoring and based on the rock mass properties presented in Table 5.

The geometry of the failure surface (red line in Fig. 7) is built according to the measurements presented in Table 2. Indeed, the dip and the crest distance are known for each profile. The dip and the distance from the slope crest to the failure surface in the upper part of each slope are in accordance with the measurements performed on each of these profiles. The lower part of each failure surface is derived by computing the failure surface with the minimal FoS that daylights at the slope toe. The global minimum approach, implemented in Slide, was used. Water was modelled as a water surface, and the Bishop simplified method of slices (25 slices) was used with a convergence tolerance of 0.005.

The results obtained are presented in Table 6. The deterministic analysis results, using average rock mass properties, are given under the column labelled FoS (deterministic). It can be seen that for sections E1, E3 and E4, the obtained FoS is close to 1 (indicative of a limit equilibrium state) and matches well with the measured failure geometry. Section E2 has a somewhat higher FoS at 1.23. Nevertheless, it appears that a reasonable fit is obtained for the investigated sections using the mean values for rock mass properties, and thus, the values given in Table 5 plausibly represent the rock mass properties.

A probabilistic analysis was then conducted using the LEA method. Monte Carlo sampling (10,000 samples) was used to assess an FoS (mean) and a probability of failure (PoF %).The running time for a probabilistic model is about 15 s on an Intel core i7 computer. As presented in Table 6, FoS (mean) and FoS (deterministic) are in the same order of magnitude. PoF is close to 50 % for sections E1 and E4, nil for section E2 and close to 30 % for section E3.

Table 6. FoS results for each profile with the LEA method

Profile	FoS (determ)	FoS (mean)	PoF (%)
E1	0.989	1.011	46.42
E2	1.229	1.278	0
E3	0.986	1.042	29.47
E4	0.971	1.009	44.47

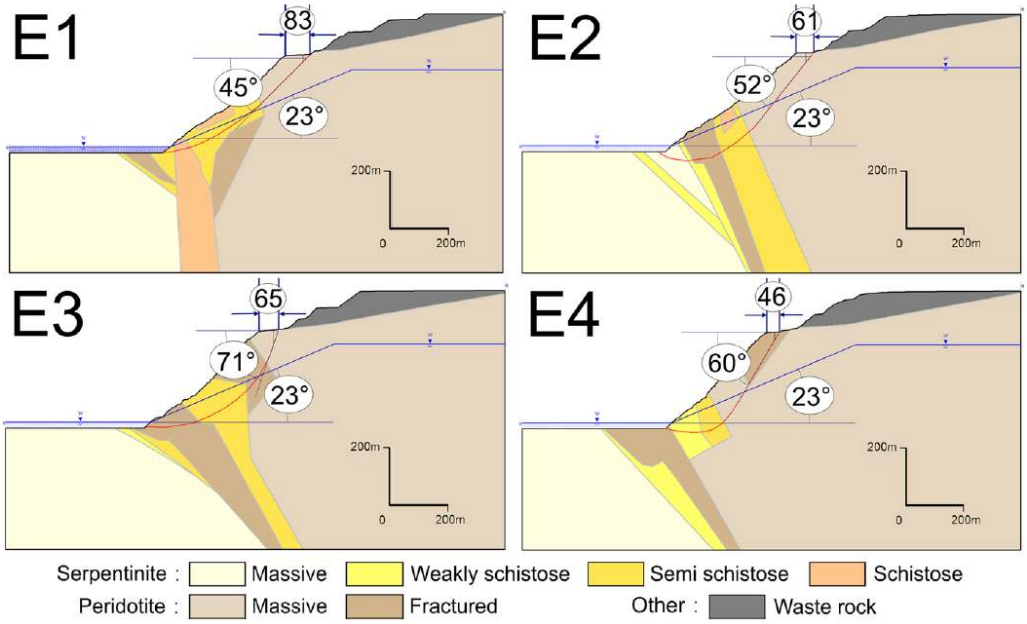

Figure 7. Geometrical characteristics for section profiles E1, E2, E3 and E4; water level in blue and initial estimation of failure surface in red (all units in metres unless stated otherwise) (colour figure online)

3.3 FE-SSR—FoS and PoF Results

This section presents a back analysis of the slope using the shear strength reduction (SSR) approach implemented in the finite-element (FE) code RS2 V9, Rocscience Inc. (2016b). The general modelling settings for FE-SSR are given in Table 7. This table is based on the work of Diederichs et al. (2007) and Hammah et al. (2005). Since the horizontal stress distribution was not known in the rock mass, it was deemed reasonable to use hydrostatic stress field conditions according to the Rocscience recommendation made in the previously mentioned papers. The models were geometrically constrained to insure that the failure surfaces would daylight at the toe of the slope.

The FoS results obtained using the average rock mass properties values are given in Table 8 under the column FoS (deterministic). The FoS values are close to 1 for sections E1, E3 and E4 and close to 1.2 for section E2. A probabilistic analysis was also performed using Monte Carlo sampling (100 runs were performed for every section). The running time for such a probabilistic model is about 3 h on an Intel core i7 computer. Because of the long running time, a more limited number of FE-SSR analyses were performed. As shown in Table 8, FoS (mean) and FoS (deterministic) are of the same order of magnitude. PoF is close to 60 % for sections E1 and E4. It is almost nil for section E2 and close to 20 % for section E3.

3.4 Discussion of LEA and FE-SSR Back Analysis Results

The results obtained by LEA and FE-SSR for the back analyses are compared in this section. FoS values obtained are very similar for all sections. The geometry of the critical failure surfaces is also very similar as shown in

Fig. 8. Both methods thus provide similar geometrical and FoS results. The FoS results for three of the investigated profiles are close to 1, thus showing clearly the critical state (stability-wise) of the slope. Profile E2 is defined with both methods (LEA and FE-SSR) with a FoS close to 1.2. These analyses also show the importance of using several cross sections when performing 2D deterministic and probabilistic numerical investigations to capture the complexity of the rock slope behaviour.

The PoF values are somewhat different for sections E1, E3 and E4 with a variation of ±14 %. PoF results are very sensitive to the mean FoS value obtained when FoS (mean) is very close to unity. This is the case for a back analysis such as the one presented in this section; thus, variations may be expected in PoF. These variations could be positive or negative. It is important to mention that the failure surfaces obtained by FE-SSR approaches are not constrained and agree very well with field observations and LEA results. At this time, full Monte Carlo FE-SSR analysis cannot be performed in 3D, thus underscoring the need to be extremely careful when performing such an analysis in 2D. Finally, it appears that the mean values obtained based on extensive field and laboratory measurements are deemed to reasonably represent the rock mass conditions at the scale of the mining slope in order to replicate the large failure that occurred in July 2012.

Table 7. General settings for all FE-SSR analyses

General	
Analysis type	Plain strain
Solver type	Gaussian elimination
Stress analysis	
Maximum number of iterations	500
Tolerance	0.001
Convergence type	Absolute energy
Mesh	
Type	Uniform
Element type	6-Node triangles
Number of mesh elements	3000
Boundary conditions	
Bottom	Restrain y
Left and right	Restrain x
Top (surface)	Free
Upper corners	Restrain x and y
Stresses	
Stress type	Gravity (using actual ground surface)
Total stress ratio (horiz/vert in plane)	1
Total stress ratio (horiz/vert out-of-plane)	1
Locked-in horizontal stresses	0
Material properties	
Initial element loading	Field stress and body force
Elastic type	Isotropic
Failure criterion	Mohr–Coulomb
Material type	Perfectly elastoplastic (peak values = residual)
Young's modulus (MPa)	100
Poisson's ratio	0.3

Table 8. FoS results for each profile with the FE-SSR method

Profiles	FoS (determ)	FoS (mean)	PoF (%)
E1	0.96	0.97	61.38
E2	1.22	1.26	0.05
E3	1.00	1.07	17.68
E4	0.97	0.99	58.56

4 WATER IMPACT DURING THE INFILLING PERIOD

The July 2012 major failure occurred after mining activity had stopped in the pit. Associated with this, pumping at the pit bottom had ceased by the end of 2011. It is known that the altitude of the water in the pit was at -14.7 m at the time of failure. This section will present a sensitivity analysis on the FoS obtained relative to the water level in the pit. The rock mass properties described in Sect. 3 will be used in this analysis. The analysis will be performed on all four sections (E1–E4) using both LEA and FE-SSR

approaches. Both analyses were performed assuming that the failure had not yet occurred, meaning it is not a post-failure analysis but rather a sensitivity analysis on the critical surface derived in Sect. 3. Figure 9 schematically presents the methodology used to investigate the impact of the infilling water in the pit.

According to Cojean and Fleurisson (1990) and Fleurisson and Cojean (2014), for a given failure surface, the rise of the water level in the pit may result at first in lowering the associated FoS until it reaches a minimum and then increases as the pit infills further. Major slope failure should be associated with water levels before the minimum is reached. This section will investigate that assumption for the present case study using both LEA and FE-SSR. It will further investigate the impact of the rise of water in the pit on the PoF computed.

4.1 LEA FoS and PoF Results

This section presents the results of deterministic and probabilistic (10,000 Monte Carlo samples) LEA analyses as implemented in Slide v7.2D, Rocscience Inc. (2016a). FoS was evaluated in all four sections for the various water levels, from a water level of -36 m (no ponded water) to a water level of 250 m. Nineteen water levels were investigated in all four sections for a total of 76 deterministic and 76 probabilistic analyses. The results are shown in Fig. 10. One can see that the FoS decreases until a water level of 10 m is reached. After that, the FoS slowly increases until the pit is totally filled. The stabilizing impact of water is obvious beyond that critical water level. This is in accordance with the work of Cojean and Fleurisson (1990) and Fleurisson and Cojean (2014). A plateau in FoS

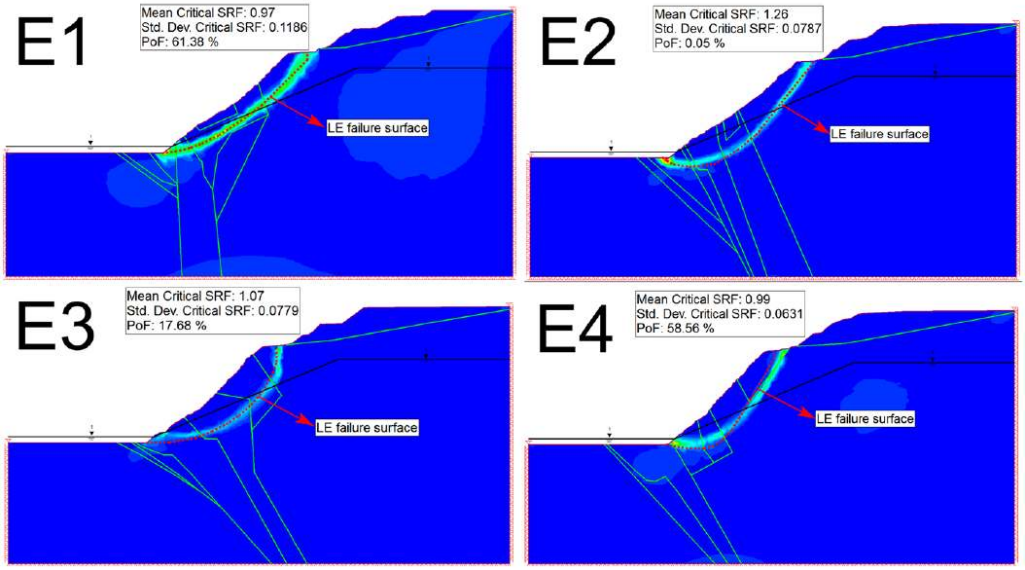

Figure 8. Comparing the back analysis results using LEA and FE-SSR methods

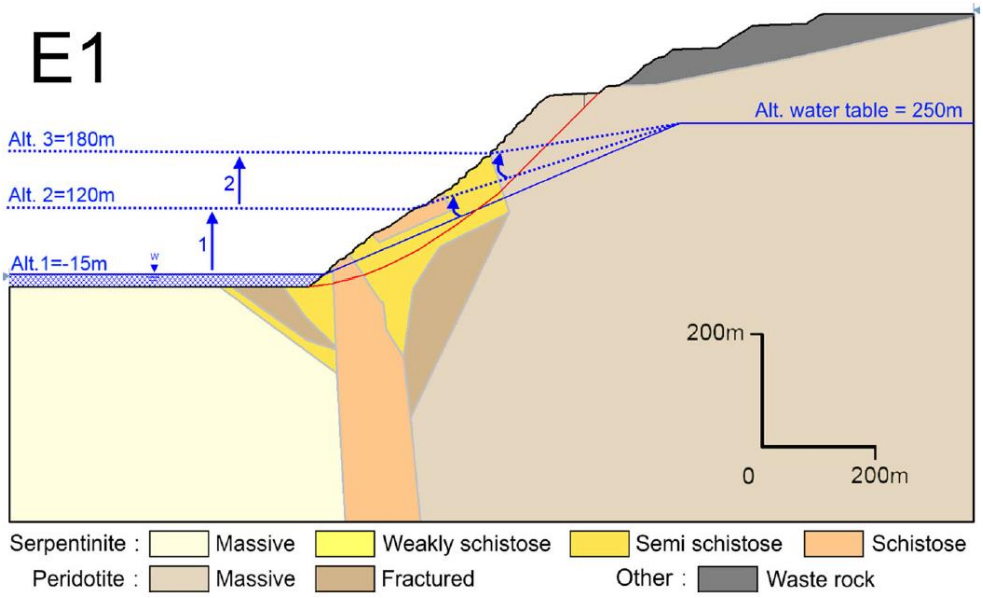

Figure 9. Assessing the impact of the water level in the pit on the FoS and PoF

values is reached between -20 and +20 m where the resulting FoS variation is at ±0.02. Since the failure occurred at a water level of -14.7 m it is justifiable to state that the slope was in its most critical state with respect to the impact of water in the pit.

A probabilistic analysis was performed using the rock mass properties shown in Table 5. For every model, the PoF was computed. Figure 10 presents the PoF results for all four sections. A similar trend is observed for the PoF as observed for the FoS. The maximum PoF is reached at a water level of 10 m. The increase in PoF is very obvious in the first part of the graph—for example, for section E4 it goes from 31 % for no ponded water to 48 % at a water level of 10 m—and then it decreases after the maximum is reached (for example, a PoF of 0 % is obtained at a water level of 150 m). This graph is another way of clearly demonstrating the findings of Cojean and Fleurisson (1990) on the early impact of the rise of water in the pit using PoF instead of FoS. In this analysis, the pit failure occurred when the PoF was very close to its maximum value.

4.2 FE-SSR Results FoS and PoF Results

This section presents the shear strength reduction (SSR) results for deterministic and probabilistic (100 Monte Carlo samples) analyses as implemented in the finite element (FE) code RS2 V9, Rocscience Inc. (2016b). Again FoS was evaluated in all four sections for the various water levels, starting at a water level of -36 m (no ponded water) and ending at a water level of 250 m. Nine water levels were investigated in all four sections for a total of 36 deterministic and 36 probabilistic analyses. The number of simulations is more limited due to computational time constraints. The results are presented in Fig. 11. One can see that the FoS decreases until a water level of 0 m to 10 m is reached for the various sections. After that, the FoS slowly increases until the pit is totally filled. A similar trend

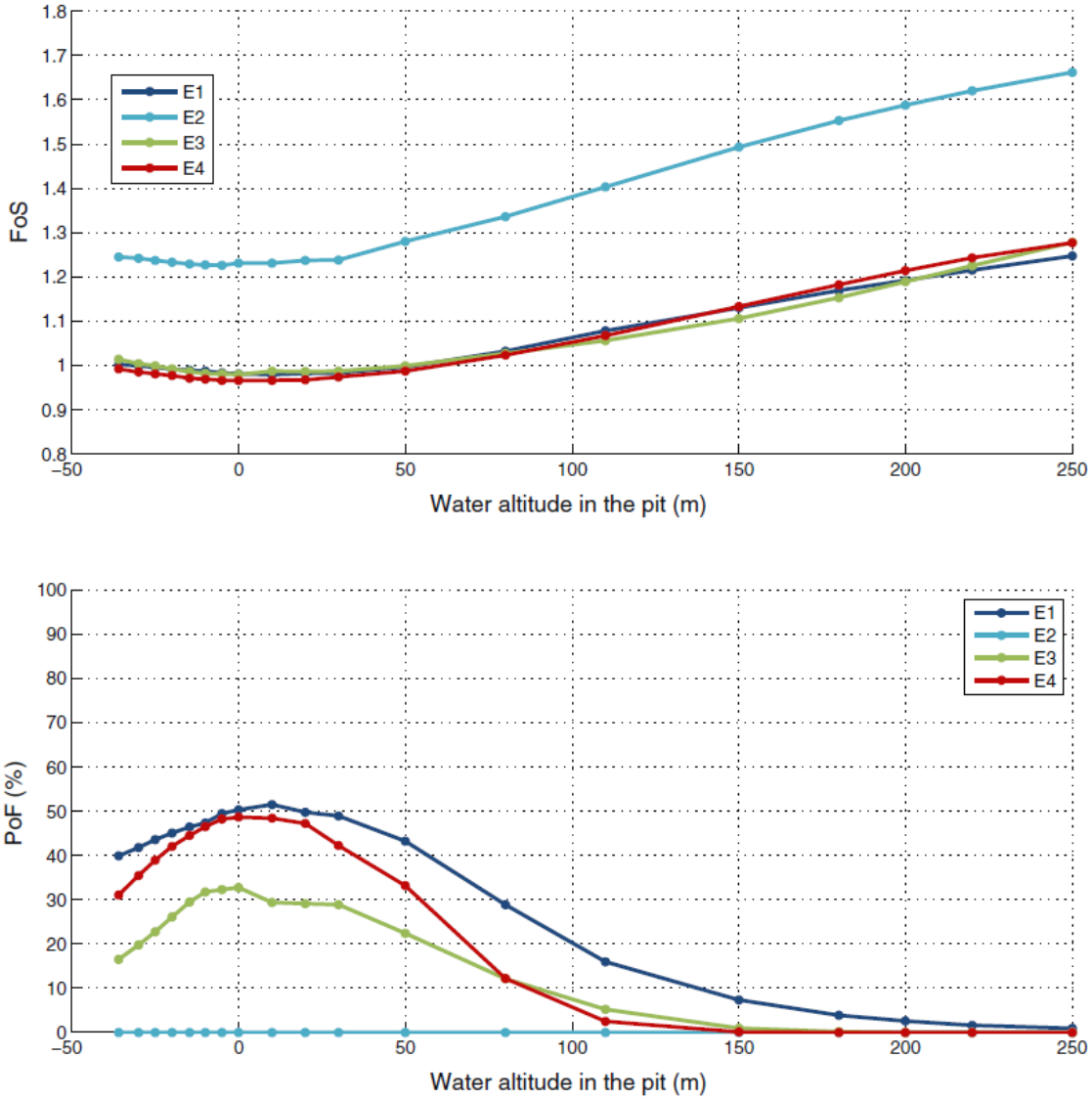

Figure 10. Variation of FoS and PoF with water altitude in the pit using deterministic and probabilistic LEA analyses

is observed for PoF: the maximum PoF is reached at a water level of 0–10 m. The increase in PoF is very obvious in the first part of the graph—for example, for section E4 it goes from 30 % for no ponded water to 65 % at a water level of 10 m—and then it decreases after the maximum is reached (for example, a PoF of 3 % at a water level of 150 m). Again in this analysis, the pit failure occurred when the PoF was very close to its maximum value.

4.3 Discussion of LEA and FE-SSR Water Impact Investigation Results

Comparing the FoS results for LEA and FE-SSR analysis in Figs. 10 and 11, one can notice that the trend and numerical values are almost identical for both methods. The curves in Fig. 11 are not as smooth as obtained in Fig. 10. This is explainable by the fact that fewer water altitudes are used and that 100 samples were used in FESSR analyses compared to 10,000 in the LEA case. The PoF results for section E2 are nil for all levels of infilled water in the pit. Larger PoF values are associated with FESSR analysis for sections E1 and E4. Smaller values in PoF are associated with FE-SSR analyses for section E3. It appears that if a PoF is higher (or lower) for a given water infilling altitude on a given section, this trend will remain the same for all investigated water level scenarios on that section. Nevertheless, the same trends are observable in PoF distributions for different water altitudes in the pit whatever the type of analysis performed (LEA or FE-SSR). Probabilistic analyses can provide a quantitative approach to assess the potential slope instability. In this case study, it clearly showed that the water level at the time of failure in July 2012 was at a critical level.

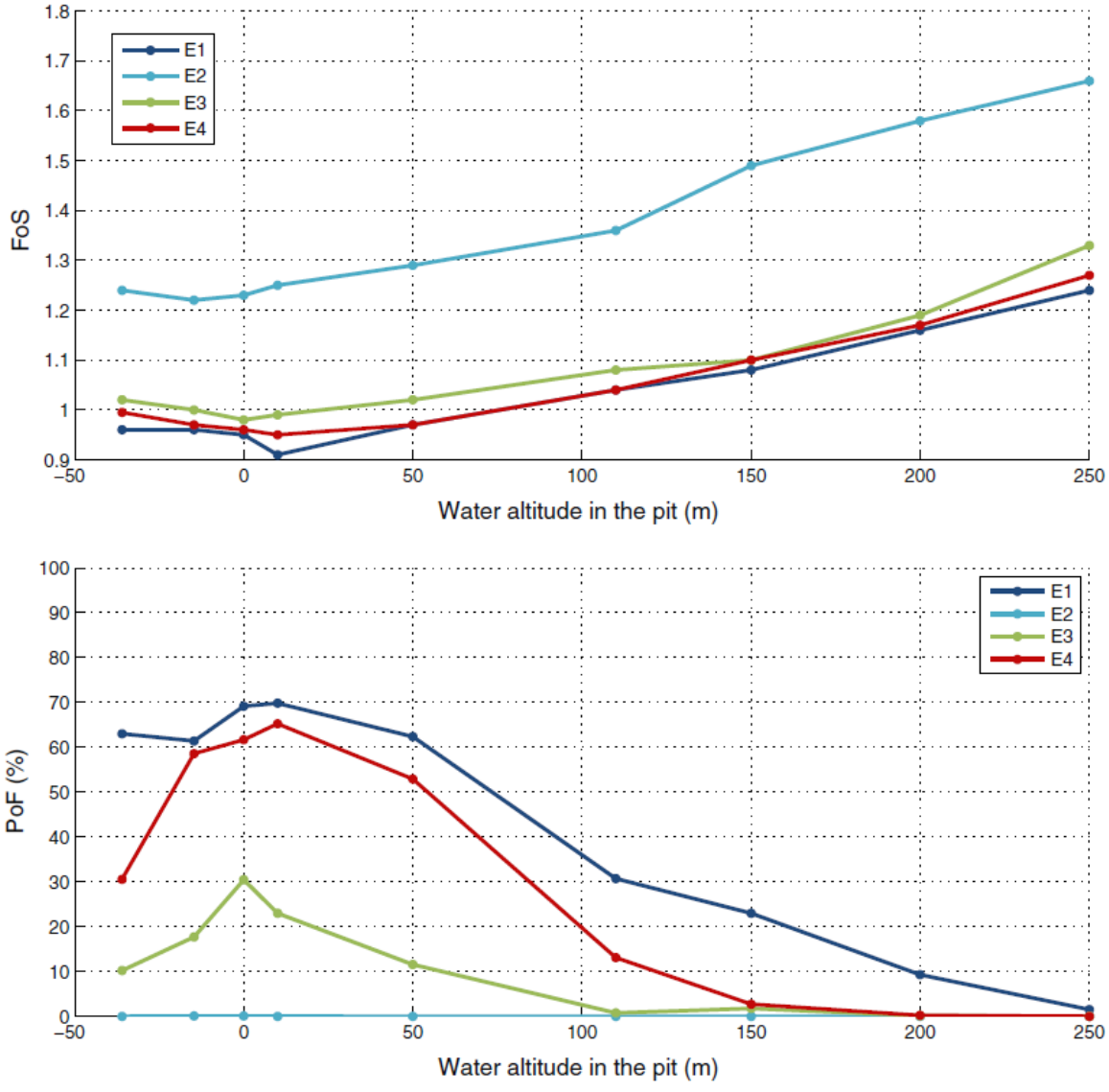

Figure 11. Variation of FoS and PoF with water altitude in the pit using deterministic and probabilistic FE-SSR analysis

5 IMPACT OF MINING ACTIVITY ON SLOPE STABILITY

In early 2010 and until 2012, the mining activity at the mine was concentrated in the lower part of the pit in the vicinity of section E1. During that period, the rock mass at the bottom of the pit was excavated. The geometry of the excavated area is presented in Fig. 12. This topography was obtained based on LiDAR scanning results. The excavation of this zone modified the slope from a global angle of 31° to a global angle of 38°. This section will investigate how the mining activity potentially impacted on the stability of the slope using both LEA and FE-SSR approaches.

The lithologies used for the 2010 slope geometry are provided and compared to the 2012 geometry in Fig. 13. The geometry of 2010 is derived from the LiDAR survey performed on 22 November 2010. The lithologies presented in 2010 were extrapolated from the lithologies used in the 2012 model.

At first, the possible extension of the critical failure surface—obtained in Sect. 3 for the 2012 slope profile—up to the toe of the new slope was investigated (Fig. 14 left). Then the model was run to derive the critical failure surface for this new geometry (Fig. 14 right).

The results for the deterministic analysis (both LEA and SSR) are presented in Table 9. The results shown for the 2012 slope geometry are simply the results presented in Sect. 3 for the back analysis. The results presented for the 2010 slope geometry show that a failure surface going through the toe of the slope and then on the critical surface derived in Sect. 3 would result in a FoS above 1.2. A more critical surface can be determined for the water condition that existed in July 2012. The results for both LEA and FESSR analyses both suggest a FoS just above 1.0 for the critical surface. When comparing the slope geometries of 2010 and 2012, the main differences in failure surfaces do not reside in the FoS results but rather in their geometries. On the 2010 slope geometry, the critical failure is daylighting 58 m above the bottom of the pit at an altitude

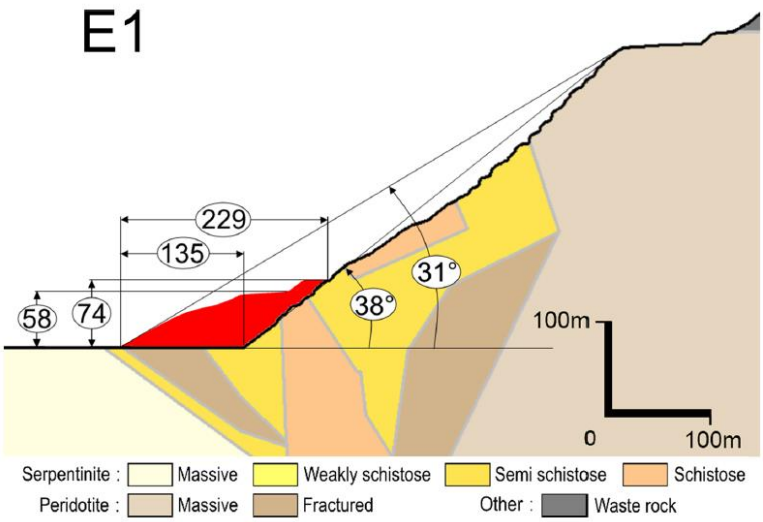

Figure 12. Slope on 29 June 2012 juxtaposed with the volume mined in 2010–2011 (in red) (all units are in metres unless stated otherwise) (colour figure online)

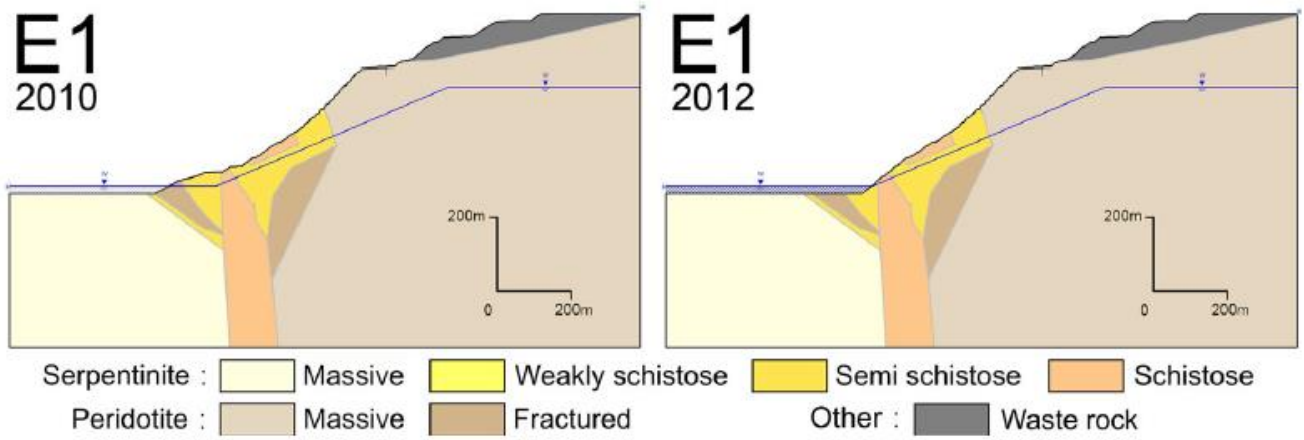

Figure 13. Geometries and lithologies of the slope for the 2010 and 2012 slope geometries

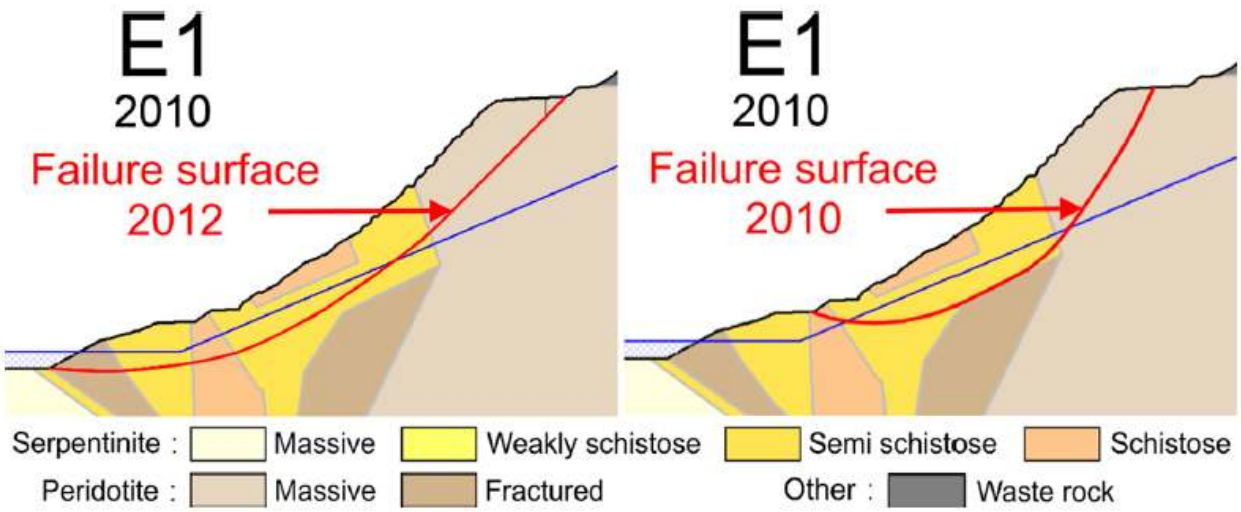

Figure 14. Left failure surface made of an extension of the 2012 failure surface obtained in Sect. 3. Right critical failure surface for the 2010 geometry

Table 9. Deterministic analysis results for LEA and FE-SSR analyses on 2010 and 2012 slope geometries for section E1 at a water altitude of -14.7 m

Slope	Analysis method			
	LEA		FE-SSR	
	Failure surface 2012	Failure surface 2010	Failure surface 2012	Failure surface 2010
Geometry of 2010	1.310	1.044	1.24	1.04
Geometry of 2012	0.989	–	0.96	

of 22 m. The critical failure surface is 80 % of the height of the critical failure surface modelled in Sect. 3 for the 2012 slope geometry.

The next step was to investigate the impact of pit infilling on the 2010 slope geometry as presented in Fig. 15. At first, deterministic and probabilistic LEA analyses were performed using the software tool Slide. The results are presented in Fig. 16 for both FoS and PoF. Thirty-eight additional deterministic and probabilistic LEA models were computed. The rock mass properties presented in Table 5 were also used in these analyses. After preliminary numerical experiments, it was deemed that for the 2010 slope geometry, the depth of failure within the various lithologies was comparable with that observed for the 2012 slope geometry. The water levels investigated are the same as were studied in Sect. 4, thus enabling easy comparison of the results. The analyses are performed for three failure surfaces: the critical one derived for the 2010 geometry (slope geometry 2010, failure surface 2010), the one associated with an extension of the 2012 failure on the 2010 geometry (slope geometry 2010, failure surface 2012) and the original 2012 failure presented in Sects. 3 and 4 (slope geometry 2012, failure surface 2012).

The FoS obtained for the 2012 geometry and the 2012 extended failure surface do not define a critical surface. The FoS obtained are always above 1.3. The presence of the abutment at the toe of section E1 results in a displacement towards the right of the curve associated with the 2010 geometry and its associated critical failure surface. The minimum FoS is reached at a water altitude in the pit of 50 m for this slope geometry failure surface configuration. The minimum FoS value is 0.983. The critical water level associated with the 2012 geometry and 2012 critical surface was 10 m with a corresponding FoS of 0.989. The minimal failure surface FoS is basically identical. Also important to note is that in both cases, the critical FoS is associated with a water level roughly 25 m above the daylight location of their respective sliding surfaces. These results thus support the findings of Cojean and Fleurisson (1990) that suggest that a minimum FoS is reached after a certain rise in the water level above the failure surface.

The same findings are observed on the PoF graph in Fig. 16. The PoF obtained for the 2012 geometry and 2012 extended failure surface does not define a critical surface. Indeed, the PoFs obtained are always equal to 0. For the 2010 slope geometry failure surface critical combination, the PoF reaches a maximum at a water level of 50 m. The variations in PoF are very obvious, increasing from 22 % for a pit with no ponded water to 50 % at a level of 50 m. These variations are exacerbated by the fact that the mean FoS is close to 1. The displacement of the curve to the right from the 2012 to the 2010 slope geometry is again obvious. The findings of Cojean and Fleurisson (1990) for the FoS are also observable—arguable even more distinctly—for the PoF values.

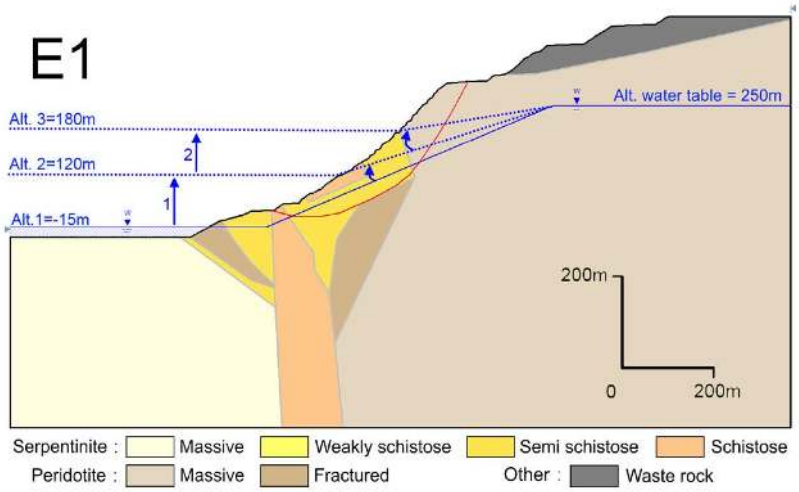

Figure 15. Assessing the impact of the water level in the pit on the FoS and PoF for the 2010 slope geometry for section E1

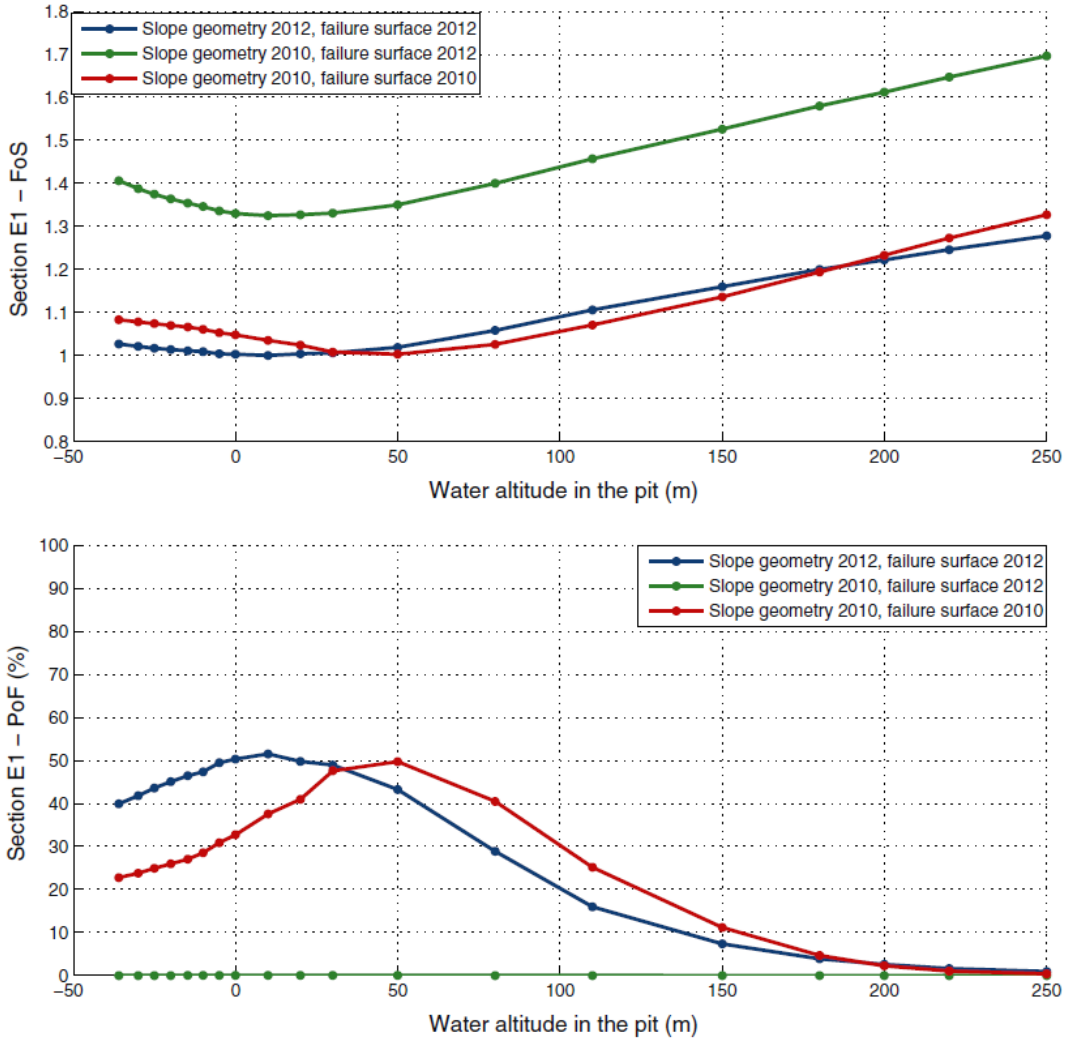

Figure 16. Variation of FoS and PoF with water altitude in the pit using deterministic and probabilistic LEA analyses for section E1 for both 2010 and 2012 slope geometries and failure surfaces

Secondly, deterministic and probabilistic FE-SSR analyses were performed using the software tool RS2. The results are presented in Fig. 17 for both FoS and PoF. Eight additional deterministic and probabilistic FE-SSR models were computed associated with the 2010 slope geometry and its associated critical failure surface. The 2010 slope geometry associated with the extended 2012 failure surface, deemed not critical in the LEA analysis, was not modelled using FE-SSR. The FoS results are comparable with those achieved for the LEA analysis. The PoF results are comparable in trend. Some small variations are observed in the numerical values when compared with the LEA analysis.

Thus, based on LEA and FE-SSR analyses, it appears that a major failure would have occurred on the 2010 geometry (with an abutment). Arguably the failure would have been smaller in size (80 % of the height) and would have happened at a later time (when the water level would have reached an altitude of 50 m). Based on LiDAR monitoring, such a water level in the pit was reached at the end of autumn 2014.

6 SUMMARY AND CONCLUSIONS

A major mining slope failure occurred in July 2012 on the East wall of the LAB Chrysotile mine in Canada. The major consequence of this failure was the loss of the local highway (Road 112), the main commercial link between the region and the Northeast USA. LiDAR scanning and subsequent analyses were performed and enabled quantifying the geometry and kinematics of the failure area. Using this information, this paper presented the back analysis of the July 2012 failure. The analyses were performed using deterministic and probabilistic limit equilibrium analysis (LEA) and finite-element shear strength reduction analysis modelling (FE-SSR). The impact of pit infilling on the stability was investigated. The impact of the mining activity in 2011 in the lower part of the slope was also investigated using a parametric analysis.

Back analysis (LEA and FE-SSR) showed that the values obtained based on extensive field and laboratory measurements were deemed appropriate to represent the rock mass conditions at the scale of the mining slope in order to replicate the large failure that occurred in July

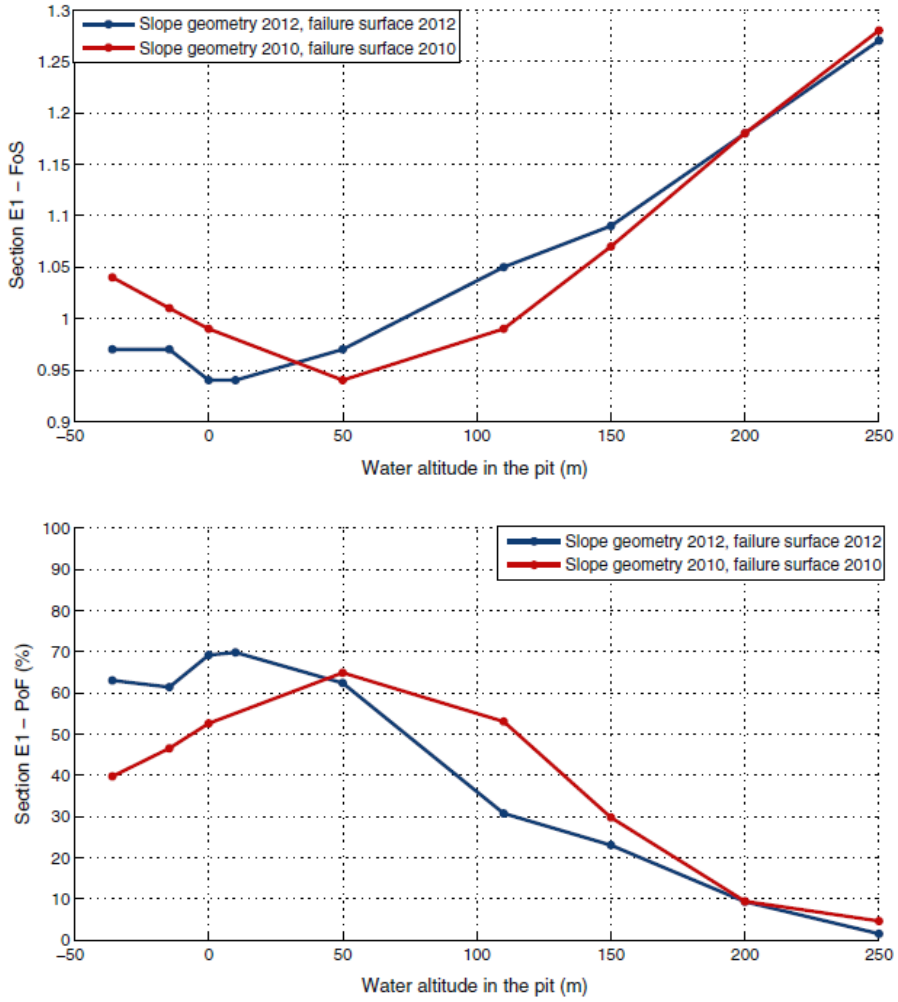

Figure 17. Variation of FoS and PoF with water altitude in the pit using deterministic and probabilistic FE-SSR analyses for section E1 for both 2010 and 2012 slope geometries and failure surfaces

2012. It also showed the advantages of having LiDAR scanning results to minimize back analysis geometrical uncertainties.

The major failure occurred after pumping at the pit bottom ceased by the end of 2011. It is known that the altitude of the water in the pit was -14.7 m at the time of failure. It appears, based on LEA and FE-SSR analyses, that such a level of water maximized the adverse effects on slope stability. FoS values obtained were at a minimum, while PoF were at a maximum. Furthermore, it was shown, for the site investigated, how the rise in infill water level can impact (positively or adversely) on the stability of a slope.

From early 2010 until 2012, mining activity at the mine was concentrated in the lower part of the pit in the vicinity of section E1. This mining activity significantly altered the geometry of the slope. Based on LEA and FE-SSR analyses, it appears that global slope instability would have been observed on the East wall of the pit even if the abutment associated with the 2010 geometry had been kept in place. Arguably the failure would have been smaller in size (80 % of the height) and would have happened later or when the infill water altitude would have reached an altitude of 50 m. Based on LiDAR monitoring, such a water level in the pit was reached at the end of autumn 2014. Nevertheless, this slope failure would have been detrimental to the perennially of Road 112.

Finally, in more general terms, this paper presented back analyses of a large slope failure. The authors used LiDAR data to acquire accurate knowledge of the pre- and post-failure slope geometry. Field and laboratory tests allowed the determination of the range in strength for the host rock masses. The paper also presented the results of using limit equilibrium analysis (LEA) and finite-element shear strength reduction analysis (FESSR) to reproduce the slope failure. It further provided the results of conducted Monte Carlo probability-of failure analyses, using both LEA and FE-SSR, to show the influence of variable strength properties, mining at the toe and a rising water table. This has led to a better understanding of the mechanism involved at the time of failure. These types of probabilistic analysis of slope failure are not routinely conducted, and the results are not interpreted to their full potential. The paper presents a unique well-documented case study that provided some valuable information on the back analysis process for large slope failures using an integrated approach relying on LiDAR scanning, laboratory testing and numerical analysis.

7 ACKNOWLEDGMENTS

The authors would like to acknowledge the financial support of Transports Québec and the Natural Sciences and Engineering Research Council of Canada (NSERC). The authors would also like to thank Pierre Dorval and François Bossé (Service Géotechnique et Géologie-Transports Québec) for providing airborne LiDAR survey data, pictures and technical advice. The authors are grateful to Michel Vallée and Gilles Bonin for providing easy mine site access. Finally, the authors are also grateful to Denis Fabre and Olivier Fouché (Conservatoire national des arts et métiers) for their technical inputs.

8 REFERENCES

Bonin G (2013) Personal communication: plan de restauration—Opération Black Lake, Instrumentation—Stabilite´ des pentes. Scale 100 = 2000. Drawn by M. N. LAB Asbestos, December 21, 2000. Sections map E1, E2, E3 et E4—Opération Black Lake— Puit Black Lake. Scale 100 = 1000. Drawn by M. N. LAB Asbestos, January 25, 2002

Caudal P (2013). Analyse d'un glissement actif par suivi LiDAR et mode´lisation de la rupture: Mine LAB Chrysotile à Black Lake, (Québec. Mémoire (diplôme ingénieur). Conservatoire national des arts et métiers, Paris

Caudal P (2015) Suivi et analyse d'un glissement actif, mur Est de la mine LAB Chrysotile à Thetford Mines. Canada, M.Sc. thesis, Université Laval

Caudal P, Grenon M, Turmel D, Locat J (2016) Analysis of large rock slope failure on the East wall of the LAB Chrysotile Mine in Canada—LiDAR monitoring and displacement analyses, Rock Mechanics and Rock Engineering. Submitted to RMRE

Cojean R, Fleurisson JA (1990) Influence de la structure géologique sur la stabilité des versants progressivement submergés par la montée d'un plan d'eau (Translation: Influence of geological structures on the stability of reservoir slopes progressively submerged by the rising water level). In: Proceedings of 6th international congress: international association of engineering geology, vol 3, Theme 4: Surface Engineering Geology

Diederichs M, Lato M, Hammah R, Quinn P (2007) Shear strength reduction approach for slope stability analyses. In: Proceedings of the 1st Canada-US rock mech symposium. Vancouver, Canada

Fleurisson JA, Cojean R (2014) Error reduction in slope stability assessment. Surface mining methods, technology and systems, vol 1

Hammah R, Yacoub T, Corkum B, Curran J (2005) A comparison of finite element slope stability analysis with conventional limit equilibrium investigation. In: Proceedings of the 58th Canadian geotechnical conference. Saskatoon, Canada

Hoek E, Carranza-Torres C, Corkum B (2002) Hoek-brown criterion— 2002 edition. Paper presented at the proceedings NARMSTAC conference 2002, Toronto, Canada

Rocscience Inc. (2016a) Slide v7.2D. Limit equilibrium slope stability analysis. www.rocscience.com. Toronto, Canada

Rocscience Inc. (2016b) RS2 v9. Finite element analysis for excavations and slopes. www.rocscience.com. Toronto, Canada

Woo K-S, Eberhardt E, Rabus B, Stead D, Vyazmensky A (2012) Integration of field characterisation, mine production and InSAR monitoring data to constrain and calibrate 3-D numerical modelling of block caving-induced subsidence. Int J Rock Mech Min Sci 53:166–178. doi:10.1016/j.ijrmms.2012.05.008